RSC Advances

This is an *Accepted Manuscript*, which has been through the Royal Society of Chemistry peer review process and has been accepted for publication.

Accepted Manuscripts are published online shortly after acceptance, before technical editing, formatting and proof reading. Using this free service, authors can make their results available to the community, in citable form, before we publish the edited article. This *Accepted Manuscript* will be replaced by the edited, formatted and paginated article as soon as this is available.

You can find more information about *Accepted Manuscripts* in the Information for Authors.

Please note that technical editing may introduce minor changes to the text and/or graphics, which may alter content. The journal's standard Terms & Conditions and the Ethical guidelines still apply. In no event shall the Royal Society of Chemistry be held responsible for any errors or omissions in this *Accepted Manuscript* or any consequences arising from the use of any information it contains.

ROYAL SOCIETY OF CHEMISTRY

www.rsc.org/advances

Seeding-induced construction of N-doped TiO_2-bronze@g-C_3N_4 two-dimensional binary nanojunctions with enhanced photocatalytic activity

Yilong Yang[a], Yongli Li[a,*], Jinshu Wang[a,*], Yan Zhang[a], Di He[a], Junshu Wu[a], Hongxing Dai[b,*]

[a] Key Laboratory of Advanced Functional Materials, School of Materials Science and Engineering, Beijing University of Technology, Beijing, 100124, China

[b] Laboratory of Green Catalysis and Separation, Key Laboratory of Beijing on Regional Air Pollution Control, and Laboratory of Catalysis Chemistry and Nanoscience, Department of Chemistry and Chemical Engineering, College of Environmental and Energy Engineering, Beijing University of Technology, Beijing 100124, China

Abstract:

Nitrogen-doped TiO_2-bronze@g-C_3N_4 (TiO_2 (B)@g-C_3N_4) two-dimensional binary heterojunctions were constructed based on seeding-induced growth through a microwave-assisted solvothermal process and subsequent thermal treatment in vacuum. The morphology of the TiO_2 (B) nanosheets could be controlled by tuning the concentration of the Ti precursor, which determined the enhanced photoelectron activity. The optimal photocatalytic activity for the degradation of methyl orange (MO) under low-intensity visible-light illumination was obtained at a TiO_2 (B)/g-C_3N_4 molar ratio of 1 : 1, which was 12.7 and 7.9 times higher than that of pure g-C_3N_4 and

RSC Advances Accepted Manuscript

P25, respectively. The photocatalytic activity was further enhanced by about 7.7 % after in situ N-doping. The improvement in photocatalytic activity of N-doped TiO_2 (B)@g-C_3N_4 hetero-nanojunctions was attributable to the strong absorption in the visible-light region and better separation of photogenerated electron/hole pairs at the nanojunction interface, a result due to the large contact area between N-doped TiO_2 (B) and g-C_3N_4 nanosheets. We have explained the photocatalytic degradation of MO molecules largely in terms of the direct oxidation by the photogenerated holes and partly by the contribution of the superoxide radicals.

Keywords: Nitrogen-doped titania-bronze, graphite-like carbon nitride, seeding-induced growth, photocatalytic dye degradation

*Corresponding authors:

Profs. Yongli Li and Jinshu Wang

E-mail addresses: lyl@bjut.edu.cn (Y. Li), wangjsh@bjut.edu.cn (J. Wang)

Prof. Hongxing Dai

E-mail address: hxdai@bjut.edu.cn

RSC Advances Accepted Manuscript

1. Introduction

Semiconductor photocatalysis has attracted much attention due to its potential environmental remediation in the degradation of organic pollutants in wastewater and the atmosphere [1,2]. Recently, graphite-like carbon nitride (g-C_3N_4), which has a delocalized conjugated π structure materials, has attracted substantial attention in visible-light-driven photocatalytic H_2 evolution and environment purification [3]. Nevertheless, rapid recombination of the photogenerated electrons and holes is a main issue limiting the practical applications of g-C_3N_4. In the past years, a number of reliable and facile strategies have been developed to fabricate modified g-C_3N_4-based photocatalysts with unique photoelectronchemical properties and photocatalytic performance, for example, protonation [4], forming porous structures [5], doping by nonmetal or metal elements [6-8], and constructing heterostructures [9-11]. Among these, coupling g-C_3N_4 with other appropriate semiconductors to construct heterostructures is an effective pathway to improve the separation of photogenerated charge carriers, resulting in an enhanced photoelectron chemical and photocatalytic performance. Recently, many heterojunction-based g-C_3N_4 materials, such as g-C_3N_4/CeO_2 [12], g-C_3N_4/MoO_3 [13], g-C_3N_4/Bi_2S_3 [14], and g-C_3N_4/ZrO_2 [15], have been reported. These materials exhibits significantly enhanced photoelectronchemical and photocatalytic activities as compared to pure g-C_3N_4. Therefore, it is envisioned that coupling g-C_3N_4 with other semiconductors might be a feasible approach to improve the visible-light harvesting efficiency and inhibit the recombination of photoexcited electron/hole pairs.

RSC Advances Accepted Manuscript

As a typical semiconductor photocatalyst, TiO_2 has been most widely investigated due to its good photocatalytic activity, low cost, and non-toxicity [3,16]. The studies on the coupling of TiO_2 with other visible-light-sensitized semiconductors have demonstrated to be an interesting way to improve its photocatalytic capability. Anatase and rutile TiO_2 have been widely studied due to their good photocatalytic performance [17-19]. TiO_2-bronze (denoted as TiO_2 (B)) is a new form of TiO_2 with a lamellar structure [20], having a large surface area, which can shorten the migration time of charge carries and suppress their recombination [21]. Since g-C_3N_4 and TiO_2 (B) have closely related structures, charge transfer is easy through the interface of the heterojunction [22,23], while multiple functionality may be promoted. To the best of our knowledge, however, there are no reports on the coupling of g-C_3N_4 with TiO_2 (B) for the photocatalytic removal of organic pollutants.

In this study, an in situ N-doped TiO_2 (B)/g-C_3N_4 two-dimensional (2D) nanojunction was fabricated via a facile microwave-assisted solvothermal route combined with a thermal treatment. The 2D structure based on the concept of seeding-induced growth. This confined the TiO_2 (B) growth on g-C_3N_4 by "seeding" its surface with microscopic nucleation sites for crystal growth in the dilute regime to reduce homogeneous nucleation. In this way a large surface area was created, which increased the contact area for adsorption of organic molecules. The photodegradation efficiency of methyl orange (MO) over the as-prepared photocatalysts was measured under visible-light irradiation. It was found that the hybrid photocatalyst decomposed MO more efficiently than the TiO_2 (B) or g-C_3N_4 sample. From these results we

RSC Advances Accepted Manuscript

propose a new photodegradation mechanism. We believe that the novel N-TiO_2 (B)@g-C_3N_4 heterostructured photocatalyst is a good candidate to be applied in environmental remediation.

2. Experimental

2.1 Photocatalyst preparation

2.1.1 g-C_3N_4 synthesis. The g-C_3N_4 powders were synthesized via the thermal polycondensation of urea according to the procedures described previously [24]. In a typical synthesis, urea (10.0 g) in a crucible was heated at a heating rate of 10 ^oC /min in a muffle furnace from room temperature (RT) to 550 ^oC and kept at thus temperature for 4 h. The resulting yellow product was collected for further use.

2.1.2 Process of "seeding" the g-C_3N_4. Titanium tetrachloride was dissolved in deionized water to form a homogeneous aqueous solution (30 μM L^{-1}). The g-C_3N_4 powders were seeded by immersion in this $TiCl_4$ aqueous solution at 70 ^oC for 60 min, followed by thoroughly washing with deionized water and drying at 80^oC for 12 h.

2.1.3 N-TiO_2 (B)@g-C_3N_4 preparation. The TiO_2 (B)@g-C_3N_4 sample was prepared using the one-step solvothermal method. 50mg g-C_3N_4 was added into 32 mL of ethylene glycol while applying ultrasonic stirring for 30 min to completely disperse the g-C_3N_4. Meanwhile, a $TiCl_4$ aqueous solution was drop wise added to the above mixture. After continuously stirring for 2 h, 1.0 mL of $NH_3 \cdot H_2O$ (25%) was added into the mixture, which was kept at 70 ^oC for 1 h. Then the mixture was transferred into a Teflon-lined autoclave and microwave-irradiated at 150 ^oC for 2 h. In the reaction process, the power of the microwave oven (XH-800C, Beijing Xianghu

RSC Advances Accepted Manuscript

Co., Ltd.) was set at 1000 W. After the autoclave was cooled to RT, the precipitate was filtered, washed with ethanol to remove the organic remnants, and dried at 50 °C overnight. The fabrication with different amounts of titanium precursors was done according to the above procedures. The TiO_2 (B)@g-C_3N_4 hybrid samples were denoted as TOCN-*X*, in which *X* was the TiO_2 (B)/g-C_3N_4 molar ratio of 0.25, 0.5, 1, and 1.5, respectively. The N-TiO_2 (B)@g-C_3N_4 (denoted as NTOCN-1) was prepared by heating the synthesized TOCN-1 at 250 °C for 2 h in vacuum. For comparison purposes, single-phase TiO_2 (B) (denoted as TO) was also prepared without g-C_3N_4 addition according to the above procedures [21].

The working electrodes were prepared as follows: 50 mg of the as-prepared photocatalyst was dispersed in 0.75 mL of ethanol to produce a slurry, which was then overlaid on a 2 cm × 4 cm fluorine-doped tin oxide (denoted as FTO) glass electrode via the doctor blading method. The electrodes were calcined at 200 °C for 10 h in air.

Urea (CH_4N_2O), ethylene glycol ($C_2H_6O_2$), tert-butyl alcohol ($C_4H_{10}O$), and triethanolamine ($C_6H_{15}NO_3$) were purchased from Sinopharm Chemical Reagent Beijing Co. Ltd. Ammonia solution ($NH_3 \cdot H_2O$) and ammonium oxalate ($(NH_4)_2C_2O_4$) were purchased from Beijing Chemical Works. Titanium tetrachloride ($TiCl_4$) was purchased from Tianjin Fuchen Chemical Reagents Factory. All chemicals were analytical grade and used as received without further purification.

2.2. Characterization

The samples were characterized using X-ray diffraction (Shimadzu XRD-7000 with Cu Kα radiation, $\lambda = 0.15418$ nm), scanning electron microscopy (Hitachi S-8020U)

RSC Advances Accepted Manuscript

and transmission electron microscopy (JEOL JEM-2010, operated at 200 KV; FEI Tecnai G2 F30, operated at 300 KV). Nitrogen adsorption−desorption isotherms and pore-size distributions were measured on a Micromeritics ASAP 2020 at −196 °C. Specific surface areas and mean pore sizes were calculated according to the BET and Barrett-Joyner-Halenda (BJH) methods, respectively. The thickness of the samples was determined by atomic force microscopy (AFM, Veeco Metrology, MultiMode-V). X-ray photoelectron spectroscopic (XPS) analysis was performed on a PHI Quantera SXM X-ray photoelectron spectrometer using the Al Kα radiation. The photoluminescence (PL) spectra of g-C_3N_4 and TiO_2 (B)@g-C_3N_4 were recorded using the Edinburgh Instruments Xe900 equipped with a xenon (Xe) lamp with an excitation wavelength of 380 nm. UV-visible (UV-vis) absorption spectra of the samples were measured on a Shimadzu-2550 UV-visible spectrophotometer. Electrochemical and photoelectrochemical activities were measured in three-electrode quartz cells with an electrochemical workstation (CHI-660D, China). 0.1 mol/L Na_2SO_4 aqueous solution was used as the electrolyte solution. A platinum electrode was used as the counter electrode, a saturated calomel electrode (SCE) was used as the reference electrodes, and g-C_3N_4 and TiO_2 (B)@g-C_3N_4 electrodes on FTO served as the working electrodes. The visible light source was a 500 W Xe lamp (CHF-XW-500W) with a 420 nm cutoff filter. The voltage over the cell was adjusted with reference to the SCE. Photoresponses of the samples with light on and light off were measured at 0 V and the electrochemical impedance spectra (EIS) were also determined at 0 V. A sinusoidal ac signal of 5 mV was applied to the electrode in the

RSC Advances Accepted Manuscript

frequency range of 1–100 KHz.

2.3. Photocatalytic evaluation

Photocatalytic activities of the samples were evaluated by measuring the decomposition of MO during the irradiation of a LED lamp (6 W, λ = 420–425 nm, about 8.0 mW cm^{-2}). 100 mg of the sample was dispersed in 100 mL of the MO aqueous solution (10 mg/L). Before illumination, the mixed solution was continuously stirred in the dark for 30 min to establish the adsorption–desorption equilibrium (Fig.S1). The concentration of the supernatant during the degradation process was measured with a UV-vis spectrometer at λ_{max}, being the wavelength that corresponds to the maximum adsorption of the dye solution. λ_{max}=505nm and the pH of the above solution was adjusted to 2.9–3.0 using H_2SO_4 to guarantee that λmax did not change. To investigate the photocatalytic mechanism of the samples, the experiments of hydroxyl radical (OH•) scavenger were carried out using 1.0 mmol tert-butyl alcohol (TBA), and hole (h^+) scavenger tests were conducted using 1.0 mmol ammonium oxalate (AO) and triethanolamine (TEOA). N_2 purging experiments were also made to confirm the results and to identify the role of superoxide species ($\bullet O_2^-$) in the photocatalysis.

3. Results and discussion

3.1. Structure and textural property

The crystal structures of the as-derived TOCN architectures were analyzed by the XRD technique, as illustrated in Fig. 1. In the XRD pattern of pure g-C_3N_4, the strongest XRD peak at 2θ = 27.7º could be indexed as the (002) diffraction plane

RSC Advances Accepted Manuscript

(JCPDS PDF# 87-1526), which was due to the long-range interplanar stacking of the conjugated aromatic system. The typical (100) peak at 2θ = 13º corresponded to an in-plane structural packing motif. The comparison of the d-spacing values between TiO_2 (B) and the JCPDS files is listed in Table 1. The XRD peaks of pure TiO_2 were in good agreement with the metastable polymorphic phase of TiO_2 (B) (JCPDS PDF# 74-1940) [24]. The diffraction peaks at 2θ = 14.2º, 24.9º, and 48.6º could be assigned to the (001), (110), and (020) planes of monoclinic TiO_2 (B), respectively. It should be noted that no phase transition occurred after calcination of the samples. As for the composite samples, the intensity of the (002) crystal plane reduced substantially by increasing the TiO_2 (B) amount. Furthermore, the characteristic XRD peak at 2θ = 27.8º, which overlapped with the diffraction peak of g-C_3N_4, could be indexed as the $(\bar{1}11)$ crystal plane of TiO_2 (B). The peak was clearly observed in the wide-scale XRD patterns of all TiO_2 (B)@g-C_3N_4 samples.

The morphology of the as-prepared TOCN samples was examined by field-emission SEM (FE-SEM) and TEM. The SEM image of g-C_3N_4 in Fig. 2a shows a clearly observable wrinkle 2D structure. Fig. 2b shows the morphology of the NTOCN-1 nanojunctions. It can be seen that TiO_2 (B) nanosheets are located on the surface of g-C_3N_4. From the high magnification image (inset of Fig. 2b), TiO_2 (B) nanosheeets are homogeneously dispersed on the surface of the building block nanosheets. The dispersion states and structures of NTOCN-1 nanojunctions can be seen in Fig. 2c and d. TiO_2 (B) displays a good distribution on the surface of g-C_3N_4, which is consistent with the SEM observations. The areas with different colors in Fig.

RSC Advances Accepted Manuscript

2c indicate the different phases, in which the nanosheets with dark color can be assigned to TiO_2 (B), whereas the gray area is ascribed to g-C_3N_4. The lattice fringes with a crystal plane distance of 0.303 nm (Fig. 2d) were attributed to the spacing of the (002) plane of TiO_2 (B). The interfaces between TiO_2 (B) and g-C_3N_4 can be seen clearly, which is a confirmation of the formation of N-TiO_2 (B)/g-C_3N_4 heterojunctions. Fig. 3 shows the AFM pattern of the N-TiO_2 (B)/g-C_3N_4 heterojunctions. 10mg NTOCN-1 sample were ultrasonic dispersed in 50mL pure ethanol, and then the solution was dropped on a monocrystalline silicon wafer. The roughness of monocrystalline silicon wafer was < 0.4 nm. As shown in Fig. 3, the morphology of NTOCN-1 confirms the SEM and TEM observations, which TiO_2 (B) nanosheeets are homogeneously dispersed on the surface of the g-C_3N_4.

Fig. S2 depicts the absorbance spectra of g-C_3N_4, TO, TOCN-1 and NTOCN-1 composites. Fig. S2 shows a clear red shift of the absorption in TOCN-1, NTOCN-1 samples, in comparison with that of TO. The as-prepared sample show obvious light absorption in visible light region due to the absorption edge of NTOCN-1 up to 450 nm, which may due to the existence of g-C_3N_4 and nitrogen species.

Textural properties of the as-prepared samples were investigated by the nitrogen adsorption–desorption measurement. The obtained sorption isotherms and BJH pore-size distributions are shown in Fig. 4. The adsorption–desorption isotherm of g-C_3N_4 has been classified as type IV with a H3 hysteresis loop, which is characteristic of mesoporous materials with slit-shaped pores [25]. TiO_2 (B) and NTOCN-1 composites also displayed typical type IV isotherms but with a H4

RSC Advances Accepted Manuscript

hysteresis loop, indicative of formation of a mesoporous structure with a slit pores (narrow pores and micropores). The surface area (S_{BET}) of TiO_2 (B) was 342 m^2/g, whereas that of pure g-C_3N_4 was 70 m^2/g. The NTOCN-1 heterostructure possessed a surface area of 312 m^2/g. The pore-size distribution curves clearly show that the NTOCN-1 material had two pore-size families located at 3.8 and 48.0 nm (Fig. 4b). These different pore sizes are attributed to released NH_3 and CO_2 bubbles that could act as the soft templates during the polymerization of urea [26] and the inter-aggregated g-C_3N_4 flakes, respectively. These results indicate that the synthesis of TiO_2 (B) on the surface of g-C_3N_4 yielded a large surface area and mesoporosity. TiO_2 (B)/g-C_3N_4 heterojunctions prepared by other molar ratios presented regular S_{BET} values, which were 277.35, 290.76 and 330.85 m^2/g for the 0.25:1, 0.5:1 and 1.5:1 molar ratio samples, respectively. As expected, the g-C_3N_4 nanosheets showed a relatively low S_{BET} of 70 m^2/g, but TiO_2 (B) was about 342 m^2/g because of the small size of the particles. It is to be expected that the S_{BET} value of TiO_2 (B)@g-C_3N_4 increased gradually by increasing the TiO_2 (B) loading. But the high S_{BET} value did not always correspond with the high catalytic activity, because the photocatalytic activity is a result of multiple effects, such as BET area and electron-hole pair separation efficiency. Although TOCN-1.5 showed the highest S_{BET} value of 330.85 m^2/g, excessive TiO_2 (B) nanoparticles aggregated seriously on the surface of g-C_3N_4 and restrained the separation of photoinduced electron-hole pairs, resulting in a low catalytic activity.

To further analyze the NTOCN-1 heterojunctions and study the interaction of TiO_2

RSC Advances Accepted Manuscript

with g-C_3N_4, XPS analysis was performed and the results are shown in Fig. 5. The C 1s spectrum (Fig. 5a) of the NTOCN-1 sample displays two peaks at binding energies (BE) = 284.48 and 288.18 eV. The peak at BE = 284.48 eV is attributed to contaminated carbon and surface carbon [27], whereas the peak at BE = 288.18 eV is assigned to C—(N)3 groups of g-C_3N_4 [28-32]. Fig. 5b is the N 1s XPS spectrum of the TOCN-1 sample. This spectrum has been fitted to four peaks, which are attributed to the sp^2-hybridized nitrogen (C—N=C) species at BE = 398.68 eV [26], the N—(C)3 species at BE = 399.76 eV [26,28,33], the quaternary N bonded to three C atoms in the aromatic cycles at BE = 401.12 eV [34] and charging effects at BE = 404.35 eV [35]. Taking into account that the BE of the incorporated N dopant in TiO_2 as interstitial N or O—Ti—N is also at 399.76 eV [33], it is obvious to assume that TiO2 is doped by N after calcination. The O 1s spectrum (Fig. 5c) of the TOCN-1 sample could be fitted to two peaks at BE = 529.78 and 531.10 eV; these peaks are due to the lattice oxygen species in TiO_2 [33] and the surface hydroxyl species [36], respectively. We also made a comparison between the Ti 2p spectra of the TOCN-1 and NTOCN-1 samples. Fig. 5d shows the Ti 2p spectra of TiO_2 in the TOCN-1 and NTOCN-1 samples. The peaks at BE = 458.48 eV (Ti $2p_{3/2}$) and 464.18 eV (Ti $2p_{1/2}$) in the TOCN-1 sample are attributed to the Ti^{4+} species in the TiO_2 clusters [37]. Interestingly, a slight shift in BE of Ti 2p in the NTOCN-1 sample was observed as compared to that in the TOCN-1 sample, suggesting that the electron density distribution changed in the Ti atoms. The negative shift in BE of Ti 2p has been ascribed to the presence of N in the TiO_2 lattice [38], because N has a N lower

RSC Advances Accepted Manuscript

electronegativity than O. This leads to the partial electron transfer from N to Ti [39]. From these considerations we conclude that N has been successfully doped into the TiO_2 lattice.

3.2. Photocatalytic performance

MO is one of the most widely used dyes with a stable azoic structure and weak adsorption on the photocatalyst surface, and therefore complete decomposition of MO is extremely difficult. For comparison purposes, Degussa P25 and the directly mixed powders of g-C_3N_4 and TiO_2 (B) with a molar ratio of 1 : 1 were also tested under the same reaction conditions. The pH value of the MO solution was adjusted to around 3 by adding a H_2SO_4 solution.

Fig. 6a shows the visible-light-driven photocatalytic activities of the g-C_3N_4-based and P25 photocatalysts for the degradation of MO. The degradation rate constant (k) was calculated from the fitted curve (Fig. 6b) according to the equation of $-\ln (C/C_0) = kt$, where C_0 represents the concentration at the adsorption–desorption equilibrium of the photocatalystbefore illumination and C the concentration at the illumination time. The result indicated that the TiO_2 (B)@g-C_3N_4 sample exhibited a higher photocatalytic activity than the pristine g-C_3N_4 and P25 samples under visible-light irradiation, implying that the photocatalytic ability of N-TiO_2 (B)@g-C_3N_4 was closely related to the TiO_2 (B) nanosheets. The photocatalytic activity of TiO_2 (B)@g-C_3N_4 increased gradually with higher TiO_2 (B) loading and reached a maximum when the TiO_2 (B)/g-C_3N_4 molar ratio was equal to 1 : 1 (TOCN-1). Moreover, the NTOCN-1 sample showed a higher photocatalytic efficiency than

RSC Advances Accepted Manuscript

TOCN-1, namely 98.6% of the MO degradation was achieved within 115 min. The apparent rate constant obtained with the NTOCN-1 sample was 0.03845 min^{-1}, which was about 1.2 times higher than that (0.03215 min^{-1}) obtained with the TOCN-1 sample and 12.7 times higher than (0.00302 min^{-1}) obtained with the g-C_3N_4 sample. The latter achieved a degradation rate of only 29.8% within 115 min. Moreover, the degradation efficiency obtained with the NTOCN-1 sample was almost 7.9 times higher than that (0.00488 min^{-1}) obtained with the P25 sample. Huang et al. studied the photoreactivity of g-C_3N_4/TiO_2(Anatase) photocatalyst prepared by a solvothermal process, and found that it was 34% higher than that of commercial P25 [13]. Yang et al. prepared C_3N_4/N-TiO_2 (mixed phases of anatase and rutile) through calcining the precursors of g-C_3N_4 and TiO_2. However, the photodegradation efficiency of representative samples was only 1.2 times higher than that of P25 [40]. The enhancement of the photocatalytic activity of our N-TiO_2 (B)@g-C_3N_4 samples might be attributed to the high efficiency of the charge separation induced by the hybrid effect of g-C_3N_4 and N-doped TiO_2. In addition, the structure of the composite might also play an important role. Firstly, the mesoporous composite displayed a large surface area, which created a large number of active sites on the surface, thereby accelerating the MO degradation rate. Secondly, the unique 2D architecture of the nanojunctions, which facilitated the transport of both photoinduced electrons and holes through the internal electrostatic field in the junction region, favored also the visible light to reach the surface and to excite the g-C_3N_4. Finally, the undoped TiO_2 in the hybrid could only absorb UV light, but N-doped TiO_2 efficiently enhanced the

RSC Advances Accepted Manuscript

visible-light absorption. The photoexcited electrons of g-C_3N_4 transferred easily to the conduction band (CB) of TiO_2 under visible-light irradiation, while the holes migrated from the valence band (VB) of TiO_2 to the VB of g-C_3N_4. Thus, the recombination of photogenerated electron/hole pairs could be significantly suppressed, with more electrons staying in the CB of TiO_2 and more holes remaining in the VB of g-C_3N_4. As the loading of TiO_2 (B) further increased, however, the degradation rate decreased. This might be attributed to the aggregation of excess TiO_2 species, which led to shielding of active sites on the g-C_3N_4 surface. This decreased the intensity of visible light through the channel to the g-C_3N_4, hence, the efficiency of charge separation was reduced. In order to show the heretojunction effect of the bronze phase on the photocatalytic activity of N-doped TiO_2 and to verify the significance of interface coupling for the photocatalytic activity of TiO_2 (B)@g-C_3N_4, the mechanically mixed g-C_3N_4 and TiO_2 sample with a TiO_2/g-C_3N_4 molar ratio of 1: 1 was used for comparison purposes. The MO photodegradation rate constant (0.01495 min^{-1}) obtained over the mixed powders was much lower than that (0.03215 min^{-1}) obtained over the TOCN-1 sample. This result indicated that the enhanced visible-light-driven photocatalytic activity of TiO_2 (B)@g-C_3N_4 came from the interface coupling. Therefore, it is crucial to inhibit the recombination of electron/hole pairs and to increase the ability for separation of photogenerated charge carriers because of the application TiO_2 (B) to the surface of g-C_3N_4.

In order to analyze the role of specific surface area and identify the effect of N doping or purposed nanojunction, we calculated the degradation rate constant (k)

RSC Advances Accepted Manuscript

divided by the S_{BET}. The values of *k* per specific surface area were $0.69*10^{-4}$ min^{-1} m^{-2} for the S-mixture sample, $1.05*10^{-4}$ min^{-1} m^{-2} for TOCN-1 and $1.23*10^{-4}$ min^{-1} m^{-2} for NTOCN-1, respectively. The highest *k* value belonged to NTOCN-1; so, it was concluded that the enhanced photocatalytic activity must be attribute to the N doping and the nanojunctions between g-C_3N_4 and TiO_2 (B).

3.3. Photochemical behavior

PL spectra of the TiO_2 (B)@g-C_3N_4 heterojunction and g-C_3N_4 samples were recorded at an excitation wavelength of 380 nm to determine the efficiency of the transfer and separation processes of photogenerated electron/hole pairs [41]. The intensity of the PL emission spectra is an indicator for the recombination level of photoexcited electron/hole pairs. The stronger the PL intensity, the higher the recombination of charge carriers [42,43]. As shown in Fig. 7a, the main emission band was centered at about 460 nm for pure g-C_3N_4, which was due to the recombination process of self-trapped excitation [44]. The emission peak positions of the TOCN-1 and NTOCN-1 samples were similar to those of the g-C_3N_4 sample. However, the emission intensity of the NTOCN-1 composite sample was lower than that of the pristine g-C_3N_4 and TOCN-1 samples. This result clearly indicates that the recombination of photogenerated charge carriers was inhibited and that both the formation of the TiO_2 (B)@g-C_3N_4 heterojunctions and N-doping into the TiO_2 lattice contributed to the separation of photoinduced charge carriers.

To further understand the photogenerated electron transfer between g-C_3N_4 and TiO_2 (B), the transient photocurrent responses of the samples that were overlaid on

RSC Advances Accepted Manuscript

the FTO electrodes were measured at pulsed illumination from a Xe lamp (λ > 420 nm). From photocurrent versus time curves (Fig. 7b) of the g-C_3N_4, TO, TOCN-1, and the NTOCN-1 composite samples with a 210 s interval in an On/Off intermittent irradiation cycle mode, one can observe that all samples exhibited fast and reproducible photocurrent response at each illumination pulse. For the NTOCN-1 sample, a sharp increase in photocurrent appeared once the Xe lamp irradiation was on, but when the irradiation was interrupted the photocurrent rapidly dropped to a steady-state value. The electrodes of these samples demonstrated a rapid photocurrent response when the light was switched back on again. The generated photocurrent was reproducible and stable during the three On/Off intermittent irradiation cycles. It can be seen that the photocurrent generated of the NTOCN-1 sample was about 1.7 and 1.3 times higher than that generated with the g-C_3N_4 and TOCN-1 samples, respectively. It is known that the higher the photocurrent, the higher the electrons/hole separation efficiency, and hence, the higher the photocatalytic activity. The enhanced photocurrent of the N-TiO_2 (B)@g-C_3N_4 sample implied that the photoinduced electron transfer was more efficient than that of the g-C_3N_4 sample: this was beneficial for enhancing the photocatalytic activity.

The electrochemical impedance spectroscopic (EIS) technique was used to analyze the charge carrier transport in the g-C_3N_4, TO, TOCN-1, and NTOCN-1 samples. In Nyquist diagrams, the radii of the arcs are associated with the charge transfer at the interface between the electrode and electrolyte solution; a small radius corresponds to a lower charge transfer resistance [45]. As shown in Fig.7c, the arc radius of the EIS

RSC Advances Accepted Manuscript

Nyquist plot of the NTOCN-1 composite sample was the smallest of all our samples at dark and irradiation conditions, demonstrating that the N-doped TiO_2 (B)@g-C_3N_4 nanojunctions exhibited the smallest charge transfer resistance. So, substantial shuttling of charges between the electrode and electrolyte and faster interfacial charge transfer occurred at the composite interface [46]. This agrees with foregoing conclusion that the enhanced coupling was due to the formation of nanojunctions and the doping of N in TiO_2.

3.4. Photocatalytic mechanism

In order to understand the photocatalytic mechanism of the heterostructured TiO_2 (B)@g-C_3N_4 samples, the active species generated during MO degradation over TiO_2 (B)@g-C_3N_4 were identified by performing the trapping and N_2 purging experiments. In this study, *t*-BuOH was used as the hydroxyl radical (•OH) scavenger [47], and ammonium oxalate (AO) and triethanolamine were used to reduce the number of holes (h^+) [48 – 52]. Superoxide radicals involved in the photodegradation could be formed according to $O_2 + e = \bullet O_2^-$ [53], so, the N_2 purging experiment was employed to identify the effect of $\bullet O_2^-$.

Fig. 8 shows the influence of various scavengers on the photocatalytic activity of the TOCN-1.5 sample for the degradation of MO. h^+ was the main active species generated in the current system, since the degradation efficiency of MO decreased significantly in the presence of AO and TEOA, in which the removal rate constant (k) decreased from 0.02074 to 0.00631 and 0.00545 min^{-1}, respectively. However, the •OH radicals were a minor active species that was auxiliary for the oxidization of MO.

RSC Advances Accepted Manuscript

For that reason the photocatalytic degradation of MO over the TOCN-1.5 sample was suppressed to a small degree after the addition of TBA to the reaction system, showing a slight influence on the *k* value (from 0.02074 to 0.01718 min^{-1}). The N_2 purging experiment in the anoxic suspension shows that near half of photocatalytic degradation rate was depressed, while 69.58 % and 73.72 % of decrease in removal rate constant were found when employing AO and TEOA as hole scavengers, respectively. These results indicate that the holes play more important role than electrons in photodegradation. In our experiments, the photoinduced electrons can transfer from the CB of g-C_3N_4 to that of TiO_2, owing to the well-matched band positions between g-C_3N_4 and TiO_2 and leading to spatial separation of photo-carriers (Fig.9). The survived electrons cannot spontaneously transfer back to the CB of g-C_3N_4, and then can be consumed by the species in the solution when there is no O_2 feeding. With sustained N_2 purging in the suspension, oxygen was almost excluded. Then the active species $\bullet O_2^-$ won't be produced without O_2 participation in the solution. Hence, the trigger of the photocatalytic activity can be attributed to the photoinduced holes. These results were also confirmed by hole-trapping experiments, because the photocatalytic activity dramatically decreased when using the hole scavengers. Therefore, although all the three reactive species, $\bullet O_2^-$, •OH and h^+, are involved in the photocatalysis, the photoinduced holes should be the greatest contributor to the oxidation of MO molecules for the TiO_2 (B)@g-C_3N_4 sample.

It is inferred from the above experimental results that the enhanced photocatalytic activity of the N-doped TiO_2 (B)@g-C_3N_4 sample is related to the following

RSC Advances Accepted Manuscript

characteristics. Fast generation of the photogenerated carriers on g-C_3N_4 and the rapid separation and transfer of these photogenerated carriers at the interface of g-C_3N_4 and TiO_2 (B) are paramount for the enhanced visible-light-driven photocatalytic performance of the TiO_2 (B)@g-C_3N_4 sample. Since the CB potential of g-C_3N_4 is more negative than that of TiO_2, the electrons can diffuse from g-C_3N_4 to TiO_2, resulting in fast transfer of negative charges from g-C_3N_4 through the nanojunction interfaces. Additionally, N-TiO_2 (B) and g-C_3N_4 possess matched Fermi levels. After visible-light irradiation, the electron that are excited to the CB of g-C_3N_4 can rapidly move to the TiO_2 (B) nanosheets, while the holes in the VB of TiO_2 (B) can migrate to g-C_3N_4, thus restraining the recombination of e_{CB}^- and h_{VB}^+ (Fig. 9). This was also supported by results of the photoelectrochemical and PL investigations.

4. Conclusions

N-doped TiO_2 (B)@g-C_3N_4 samples have been successfully prepared based on the seeding-induced growth through a facile solvothermal process. The N-TiO_2 (B)@g-C_3N_4 samples exhibited significantly enhanced visible-light-driven photocatalytic activity, about 12.7 and 7.9 times higher than the g-C_3N_4 and P25 samples, respectively, which were attributed to the effective utilization of visible light due to N-doping and high separation efficiency of the photogenerated electron/hole pairs at the heterojunction interfaces. The seeding-induced growth was important in building the 2D binary structured photocatalytic materials and this strategy is expected to be extended for depositing other components on the surface of g-C_3N_4.

RSC Advances Accepted Manuscript

Acknowledgements

This work was supported by the National Natural Science Foundation (no. 51471006, 51225402), Beijing Natural Science Foundation（no.2151001） and Guangxi Natural Science Foundation (no.2014GXNSFBA118039).

References

1 M.R. Hoffmann, S.T. Martin, W.Y. Choi, D.W. Bahnemann, *Chem. Rev.*, 1995, **95**, 69−96.

2 A. Mills, S.L. Hunte, *J. Photochem. Photobiol. A*, 1997, **108**, 1−35.

3 D. Dvoranova, V. Brezova, M. Mazur, M.A. Malati, *Appl. Catal. B*, 2002, **37**, 91−105.

4 M. Tahir, C.B. Cao, N. Mahmood, F.K. Butt, A. Mahmood, F. Idrees, S. Hussain, M. Tanveer, Z. Ali, I. Aslam, *Appl. Mater. Interfaces*, 2014, **6**, 1258−1265.

5 K. Kailasam, J. D. Epping, A. Thomas, S. Losse, H. Junge, *Energy Environ. Sci.*, 2011, **4**, 4668−4674.

6 J. Zhang, M. Zhang, G. Zhang, X. Wang, *ACS Catal.*, 2012, **2**, 940−948.

7 X.C. Wang, X.F. Chen, A. Thomas, X.Z. Fu, M. Antonietti, *Adv. Mater.*, 2009, **21**, 1609−1612.

8 Z. Ding, X. Chen, M. Antonietti, X. Wang, *ChemSusChem*, 2011, **4**, 274−281.

9 Y.J. Wang, R. Shi, J. Lin, Y.F. Zhu, *Energy Environ. Sci.*, 2011, **4**, 2922−2929.

10 Y.J. Wang, X.J. Bai, C.S. Pan, J. He, Y.F. Zhu, *J. Mater. Chem.*, 2012, **22**, 11568−11573.

11 C.S. Pan, J. Xu, Y.J. Wang, D. Li, Y.F. Zhu, *Adv. Funct. Mater.*, 2012, **22**,

RSC Advances Accepted Manuscript

1518−1524.

12 L.Y. Huang, Y.P. Li, H. Xu, Y.G. Xu, J.X. Xia, K. Wang, H.M. Li and X.N. Cheng, *RSC Adv.*, 2013, **3**, 22269-22279.

13 Y.M. He, L.H. Zhang, X.X. Wang, Y. Wu, H.J. Lin, L.H. Zhao, W.Z. Weng, H.L. Wan and M.H. Fan, *RSC Adv.*, 2014, **4**, 13610-13619.

14 X.S. Rong, F.X. Qiu, J. Yan, H. Zhao, X.L. Zhu and D.Y. Yang, *RSC Adv.*, 2015, **5**, 24944-24952.

15 X.X. Wang, L.H. Zhang, H.J. Lin, Q.Y. Nong, Y. Wu, T.H. Wu and Y.M. He, *RSC Adv.*, 2014, **4**, 40029-40035.

16 S. Yin, H. Yamaki, M. Komatsu, Q.W. Zhang, J.S. Wang, Q. Tang, F. Saito, T. Sato, *J. Mater. Chem.*, 2003, **13**, 2996−3001.

17 D.O. Scanlon, C.W. Dunnill, J. Buckeridge, S.A. Shevlin, A.J. Logsdail, S.M. Woodley, C.R.A. Catlow, M.J. Powell, R.G. Palgrave, I.P. Parkin, G.W. Watson, T.W. Keal, P. Sherwood, A. Walsh, A.A. Sokol, *Nat. Mater.*, 2013, **12**, 798−801.

18 J.S. Wang, H. Li, H.Y. Li, C. Zou, H. Wang, D.S. Li, *ACS Appl. Mater. Interfaces*, 2014, **6**, 1623−1631.

19 J.Y. Liao, B.X. Lei, H.Y. Chen, D.B. Kuang, C.Y. Su, *Energy Environ. Sci.*, 2012, **5**, 5750−5757.

20 R. Marchand, L. Brohan, M. Tournoux, *Mater. Res. Bull.*, 1980, **15**, 1129−1133.

21 G.L. Xiang, T.Y. Li, J. Zhuang, X. Wang, *Chem. Commun.*, 2010, **46**, 6801−6803.

22 M. Li, X.F. Yu, S. Liang, X.N. Peng, Z.J. Yang, Y.L. Wang, Q.Q. Wang, *Adv. Funct. Mater.*, 2011, **21**, 1788−1794.

RSC Advances Accepted Manuscript

23 X. Chen, S. Shen, L. Guo, S.S. Mao, *Chem. Rev.*, 2010, **110**, 6503–6570.

24 J.H. Liu, T.K. Zhang, Z.C. Wang, G. Dawson, W. Chen, *J. Mater. Chem.*, 2011, **21**, 14398–14401.

25 K. S. W. Sing, D. H. Everett, R. A. W. Haul, L. Moscou, R. A. Pierotti, J. Rouquerol, T. Siemieniewska, *Pure & Appl. Chem.*, 1985, **57**, 603—619.

26 Y.W. Zhang, J.H. Liu, G. Wu, W. Chen, *Nanoscale*, 2012, **4**, 5300–5303.

27 C. Li, C.B. Cao, H.S. Zhu, *Mater. Lett.*, 2004, **58**, 1903–1906.

28 C. Mirand, H. Mansilla, J. Yáñez, S. Obregón and G. Colóna, *J. Photochem. Photobiol. A*, 2013, **253**, 16–21.

29 A. Thomas, A. Fischer, F. Goettmann, M. Antonietti, J. Muller, R. Schlogl, J.M. Carlsson, *J. Mater. Chem.*, 2008, **18**, 4893–4908.

30 V.N. Khabashesku, J.L. Zimmerman, J.L. Margrave, *Chem. Mater.*, 2000, **12**, 3264–3270.

31 C. Li, X. Yang, B. Yang, Y. Yan, Y. Qian, *Mater .Chem. Phys.*, 2007, **103**, 427–432.

32 Q. Guo, Y. Xie, X. Wang, S. Lv, T. Hou, X. Liu, *Chem. Phys. Lett.*, 2003, **380**, 84–87.

33 B. Chai, T. Peng, J. Mao, K. Li, L. Zan, *Phys. Chem. Chem. Phys.*, 2012, **14**, 16745–16752.

34 D. Gao, Q. Xu, J. Zhang, Z. Yang, M. Si, Z. Yan, D. Xue, *Nanoscale*, 2014, **6**, 2577–2581.

35 S.C. Yan, Z.S. Li, Z.G. Zou, *Langmuir*, 2010, **26**, 3894–3901.

36 G.S. Shao, T.Y. Ma, X.J. Zhang, T.Z. Ren, Z.Y. Yuan, *J. Mater. Sci.*, 2009, **44**,

RSC Advances Accepted Manuscript

6754−6763.

37 X. Zhou, F. Peng, H. Wang, *Chem. Commun.*, 2011, **47**, 10323−10325.

38 S. Zhou, Y. Liu, J.M. Li, Y.J. Wang, G.Y. Jiang, Z. Zhao, D.X. Wang, A.J. Duan, J. Liu, Y.C. Wei, *Appl. Catal. B*, 2014, **158**, 20–29

39 K.M. Parida, S. Pany, B. Naik, *Int. J. Hydrogen Energy*, 2013, **38**, 3545−3553

40 N. Yang, G.Q. Li, W.L. Wang, X.L. Yang, W.F. Zhang, *J. Phys. Chem. Solids*, 2011, **72**, 1319−1324.

41 S. Martha, A. Nashim, K.M. Parida, *J. Mater. Chem. A*, 2013, **1**, 7816−7824.

42 D. Jiang, L. Chen, J. Zhu, M. Chen, W. Shi, J. Xie, *Dalton Trans.*, 2013, **42**, 15726−15734.

43 J. Cao, B.D. Luo, H.L. Lin, B.Y. Xu, S.F. Chen, *Appl. Catal. B*, 2012, **111-112**, 288-296.

44 C. Han, L. Ge, C. Chen, Y. Li, X. Xiao, Y. Zhang, L. Guo, *Appl. Catal. B*, 2014, **147**, 546−553.

45 Y. Hou, F. Zuo, A. Dagg, P. Feng, *Angew. Chem. Int. Ed.*, 2013, **52**, 1248−1252.

46 Y. Hou, F. Zuo, A. Dagg, P. Feng, *Nano Lett.*, 2012, **12**, 6464−6473.

47 H. Lee, W.Y. Choi, *Environ. Sci. Technol.*, 2002, **36**, 3872−3878.

48 X.C. Wang, K. Maeda, A. Thomas, K. Takanabe, G. Xin, J. M. Carlsson, K. Domen, M. Antonietti, *Nat. Mater.*, 2009, **8**, 76−80.

49 Y. Zhang, N. Zhang, Z.R. Tang, Y.J. Xu, *Chem. Sci.*, 2012, **3**, 2812−2822.

50 W. Li, D. Li, Y. Lin, P. Wang, W. Chen, X. Fu, Y. Shao, *J. Phys. Chem. C*, 2012, **116**, 3552−3560.

RSC Advances Accepted Manuscript

51 Y. Zhang, N. Zhang, Z.R. Tang, Y.J. Xu, *ACS Nano*, 2012, **6**, 9777–9789.

52 X. Wang, K. Maeda, X. Chen, K. Takanabe, K. Domen, Y. Hou, X. Fu, M. Antonietti, *J. Am. Chem. Soc.*, 2009, **131**, 1680−1681.

53 J. Kim, C.W. Lee, W. Choi, *Environ. Sci. Technol.*, 2010, **44**, 6849–6854.

RSC Advances Accepted Manuscript

Table 1. Comparison of the d-spacing values between NTOCN-1 and the JCPDS files.

	TiO_2(B): JCPDS PDF# 74-1940		
	(h k l)	2-Theta	d-spacing
JCPDS	001	14.186º	0.6238nm
	110	24.979º	0.3561nm
	$\bar{1}11$	27.681º	0.322nm
	002	28.596º	0.311nm
	020	48.634º	0.187nm
	Sample		
NTOCN-1	001	14.2 º	0.617nm
	110	24.9 º	0.345nm
	$\bar{1}11$	27.8 º	0.320nm
	002	28.62º	0.303nm
	020	48.6 º	0.190nm

RSC Advances Accepted Manuscript

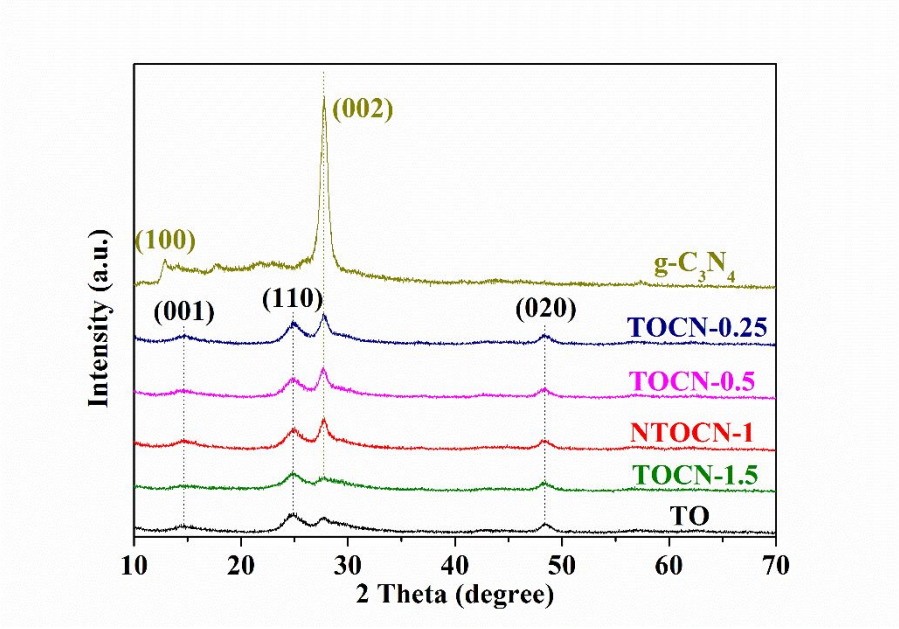

Fig. 1. XRD patterns of the g-C_3N_4, TO, and TOCN samples.

RSC Advances Accepted Manuscript

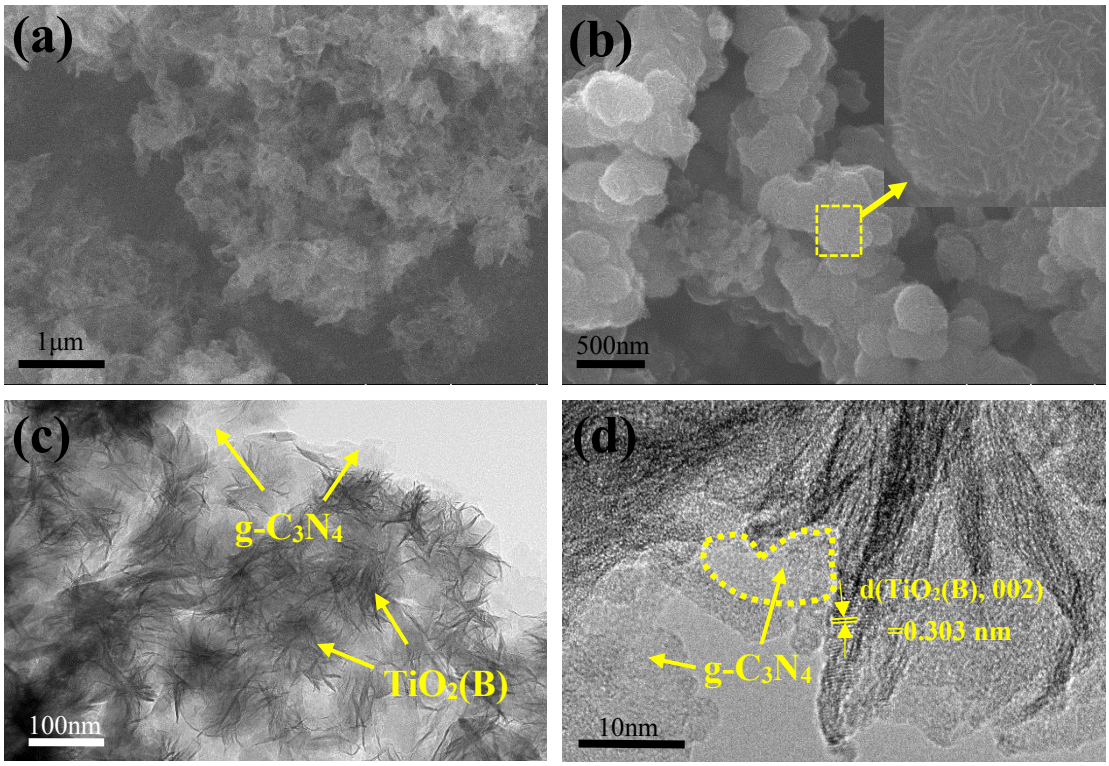

Fig. 2. Typical FE-SEM (a) image of g-C_3N_4 and SEM (b), TEM (c), and STEM (d) images of the NTOCN-1 sample.

RSC Advances Accepted Manuscript

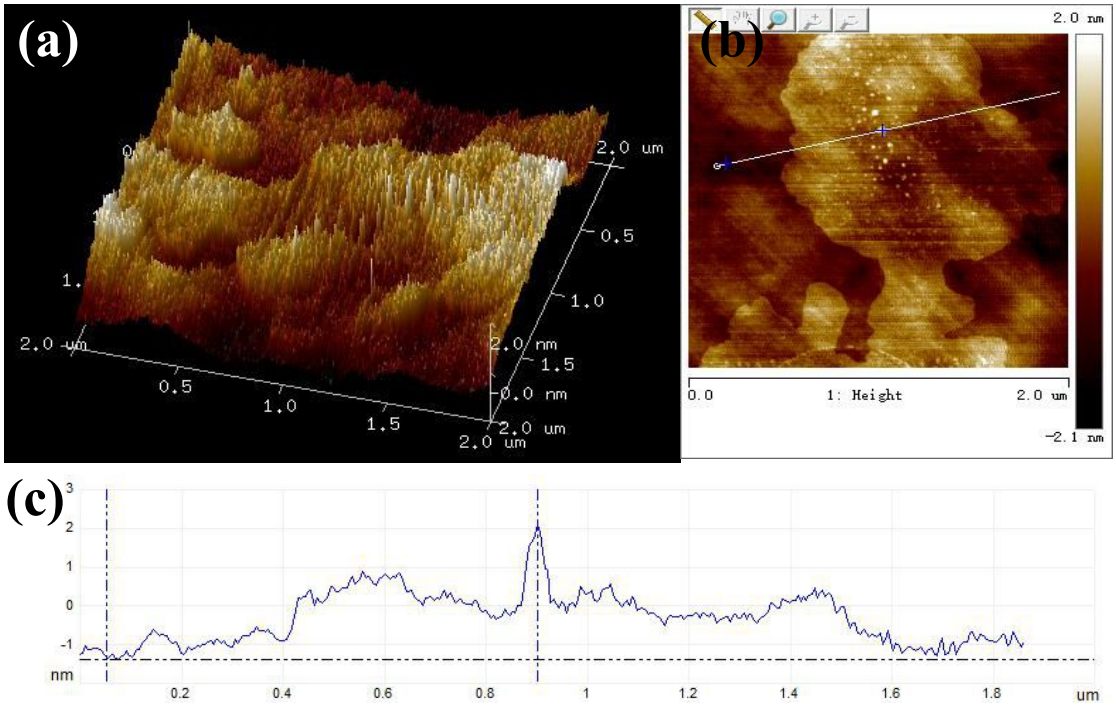

Fig. 3. AFM pattern of the NTOCN-1 sample.

RSC Advances Accepted Manuscript

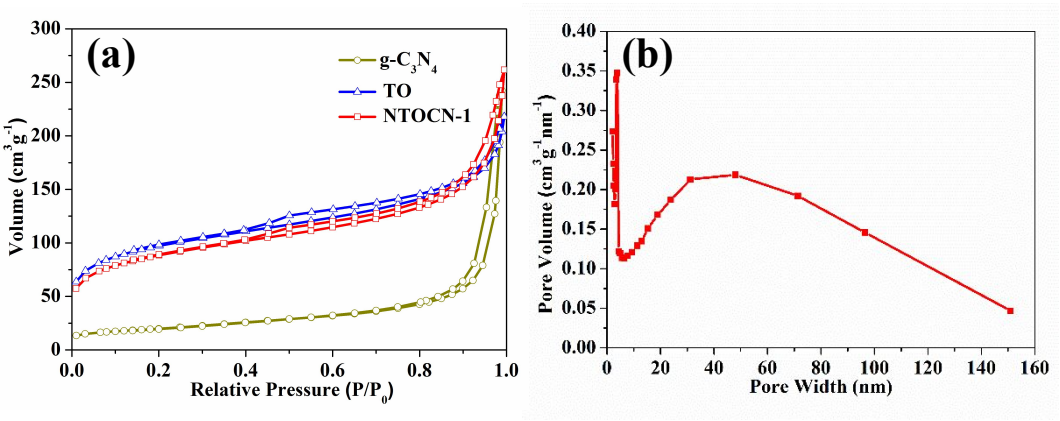

Fig. 4. N_2 adsorption–desorption isotherms of (a) the representative samples and (b) pore-size distribution of the NTOCN-1 sample.

RSC Advances Accepted Manuscript

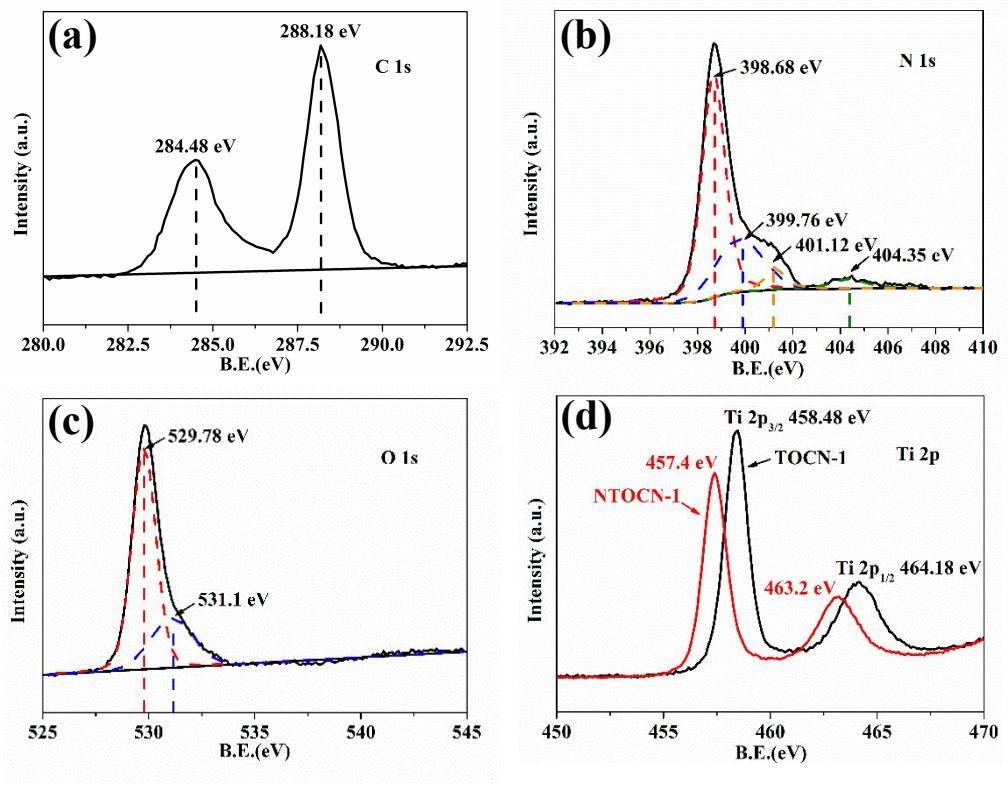

Fig. 5. (a) C 1s, (b) N 1s, (c) O 1s, and (d) Ti 2p XPS spectra of the typical samples.

RSC Advances Accepted Manuscript

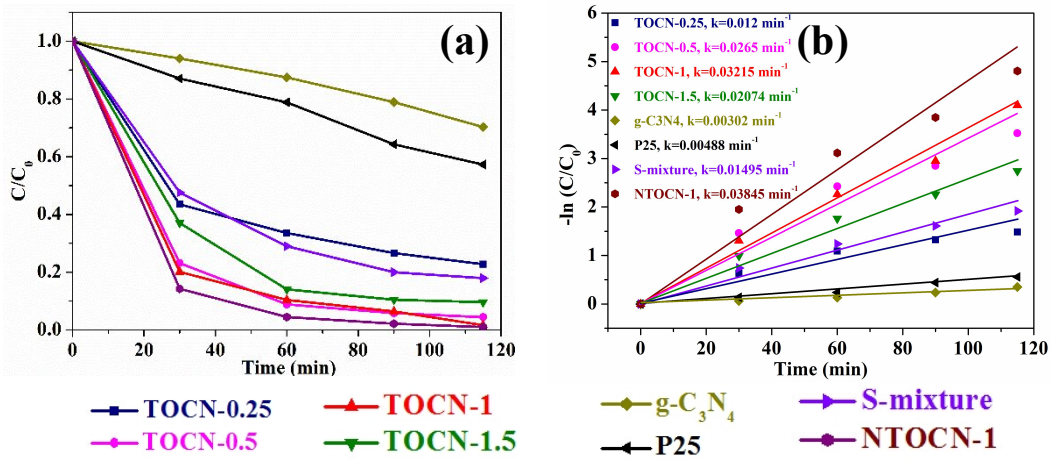

Fig. 6. (a) Photocatalytic degradation efficiency of MO over the typical samples under 420 nm LED light irradiation and (b) the pseudo-first-order rate constant *k* obtained over the different samples.

RSC Advances Accepted Manuscript

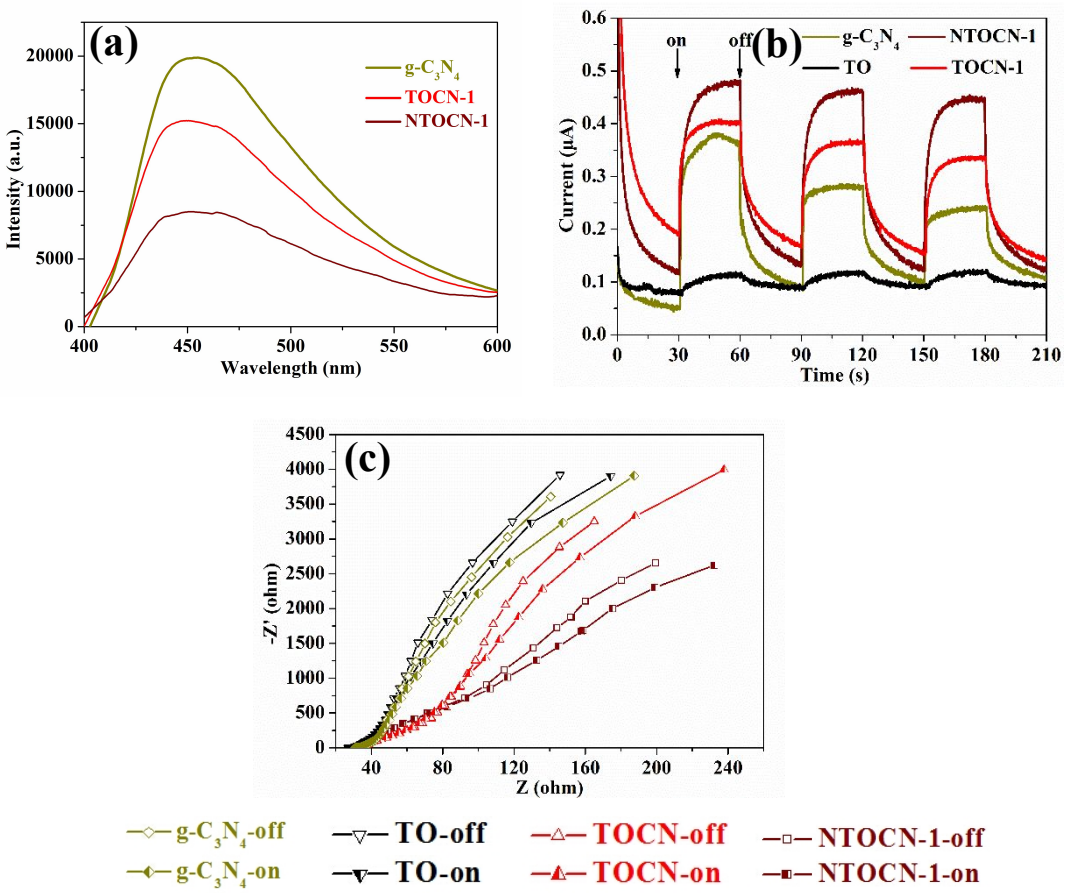

Fig. 7. (a) Photoluminescence spectra of g-C_3N_4, TOCN-1, and NTOCN-1 nanojunctions, (b) transient photocurrent density versus time of g-C_3N_4, TO, TOCN-1, and NTOCN-1 nanojunctions, and (c) EIS Nyquist plots of g-C_3N_4, TO, TOCN-1, and NTOCN-1 nanojunctions.

RSC Advances Accepted Manuscript

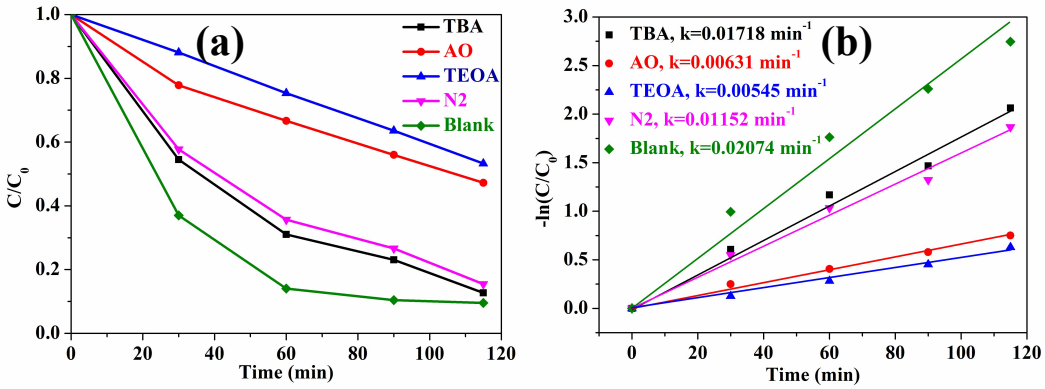

Fig. 8. (a) Influence of various scavengers on the visible-light-driven photocatalytic activity of TOCN-1.5, and (b) apparent rate constants obtained over TOCN-1.5 for MO degradation under visible-light irradiation.

RSC Advances Accepted Manuscript

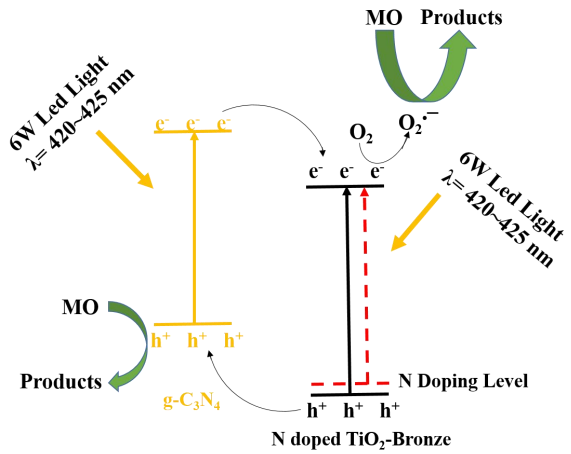

Fig. 9. Schematic illustration of the photocatalytic mechanism over the N-TiO_2 (B)@g-C_3N_4 composite sample under visible-light irradiation.

RSC Advances Accepted Manuscript

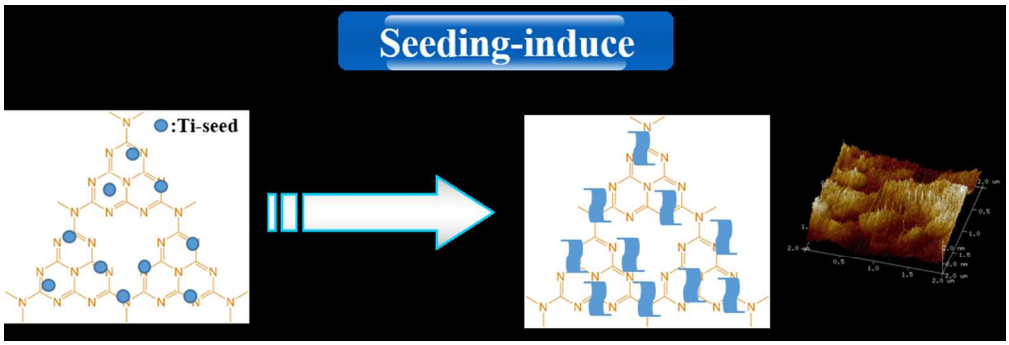

179x60mm (150 x 150 DPI)

RSC Advances Accepted Manuscript